energies

MDPI

*Article*

# Research on the Energy Conversion Mechanism of Engine Speed, Turbulence and Combustion Stability Based on Large Eddy Simulation

**Zijian Zhang [1], Milan Cheng [1], Hui Wang [2], Shengkai Zhou [2,3], Song Zhang [2], Mingzhang Pan [1,3], Wei Guan [1], Mantian Li [1] and Hailang Sang [2,3,*]**

[1] College of Mechanical Engineering, Guangxi University, Nanning 530004, China
[2] Guangxi Yuchai Machinery Group Co., Ltd., Yulin 537000, China
[3] State Key Laboratory of Engines, Tianjin University, Tianjin 300072, China
* Correspondence: sanghail@yuchai.com

**Abstract**

Cycle-to-cycle variation (CCV) is an inherent phenomenon in internal combustion engines that poses significant limitations on thermal efficiency in energy conversion. This variation can also cause structural damage. Other negative effects include increased noise and elevated emissions. This research employs large eddy simulation (LES) coupled with the G-equation model and detailed SAGE chemistry to investigate the impact of varying engine speeds on cyclic variability and energy conversion, which focuses specifically on CCV phenomena. Unlike previous studies that focus primarily on statistical pressure variations, this work uncovers the causal link between the initial flame kernel morphology and the propensity for end-gas auto-ignition. The results demonstrate that increasing engine speed significantly enhances in-cylinder turbulence intensity. Specifically, the maximum turbulence energy at 5000 rpm is about 85% higher than that at 4000 rpm. The maximum turbulence energy at 4000 rpm is about 103% higher than that at 3000 rpm. Speed alterations also change the initial conditions of temperature and fuel distribution that have a major impact on CCV characteristics. As engine speed increases from 3000 rpm to 5000 rpm, the coefficient of variation in the maximum peak pressure decreases from 14.9% to 9.48%. The coefficient of variation follows a decreasing then increasing trend with the values ranging from 7.8% to 8.1%. While a moderate increase in engine speed can reduce peak pressure fluctuation and improve combustion stability, excessively high speeds may induce delayed flame propagation and instability in kernel development, which can exacerbate the combustion phasing variations. The propensity for exhaust gas auto-ignition near the intake valve increases to raise the risk of engine knocking. Our research findings underscore the critical balancing role of engine speed in optimizing energy conversion and provide a basis for mitigating engine knock.

**Keywords:** internal combustion engine; cycle-to-cycle variation; large eddy simulation; computational fluid dynamics; flame kernel; turbulence

Check for updates

Academic Editor: Roberto Finesso

Received: 16 November 2025
Revised: 12 December 2025
Accepted: 16 December 2025
Published: 29 December 2025

**Copyright:** © 2025 by the authors. Licensee MDPI, Basel, Switzerland. This article is an open access article distributed under the terms and conditions of the Creative Commons Attribution (CC BY) license.

## 1. Introduction

To ensure sustainable development and meet the international requirements for net-zero emissions, many studies are dedicated to researching clean energy sources such as electric fuels and biofuels for engines [1]. However, vehicles powered by internal combustion engines still occupy the majority of the current market [2]. The use of traditional fossil

fuels will inevitably cause climate change and air pollution. However, human development still relies on fossil fuels [3,4]. To achieve the dual goals of energy conservation and emission reduction, some countries or regions are actively promoting the use of emerging clean fuels or advanced internal combustion engine technologies [5,6]. The appropriate combustion parameters selected to control internal combustion engines can enhance their performance [7]. Therefore, understanding the mechanism and characteristics of internal combustion engine combustion has strong practical significance in this context. More powerful performance and better fuel economy can be achieved by increasing the compression ratio and pressure of the internal combustion engine and downsizing the engine. Therefore, it is regarded as an effective way to improve the thermal efficiency of the internal combustion engine. However, the knocking phenomenon of the engine will be exacerbated in this case [8]. When an internal combustion engine is in operation, it is inevitable that there will be CCV phenomena. CCV refers to the random variation phenomenon of combustion process parameters in a spark ignition engine under constant working conditions among continuous working cycles. However, it can adversely affect engine performance when this phenomenon intensifies [9,10]. Overall, the ability to characterize the combustion characteristics of internal combustion engines is crucial for the reliability, efficiency, and emissions performance [11].

In order to gain a deeper understanding of the combustion mechanism, many researchers have performed a lot of work on the CCV and knocking phenomena of internal combustion engines. Extensive research has been conducted to understand the mechanisms of CCV and knock. Numerical studies using RANS and LES have been widely employed to analyze the impact of flame kernel growth and air-fuel ratio fluctuations on cyclic variability [12–15]. Additionally, data-driven approaches such as machine learning have recently been applied to classify combustion states [16]. According to the research of Ding et al., the method using LES can effectively capture the CCV of internal combustion engines, thereby quantifying its impact on combustion [17,18]. LES can analyze the key factors influencing flame generation and growth in internal combustion engines [19], thereby being able to reproduce the observed cyclic variation phenomena with high fidelity at both quantitative and qualitative levels [14]. Therefore, LES can still play a crucial role in revealing the physical mechanism of CCV in internal combustion engines.

CCV and knocking interact in a complex feedback loop, where stochastic combustion variations persist even under strictly controlled operating conditions [20,21]. Understanding these variations is critical for optimizing engine efficiency and emissions [22]. While Deng et al. [23] identified rotational speed as a dominant factor governing CCV, the fundamental physical mechanisms underlying this dominance, particularly the specific interactions between turbulence and flame propagation, remain to be fully elucidated.

Cycle-to-cycle variability (CCV) in internal combustion engines can be investigated by observing flame combustion and fluctuation phenomena via transparent components or optical engines [24]. Since ICE performance is intrinsically linked to in-cylinder combustion conditions [25], parameters such as cylinder pressure and crank angle are also utilized to quantify CCV [26]. By evaluating various metrics, it is possible to determine the optimal operating conditions required to minimize CCV [27]. Furthermore, the identification and characterization of CCV can be achieved by employing numerical simulations to generate massive datasets, which are subsequently analyzed using clustering algorithms or other data-driven methodologies [28,29]. Currently, integrating advanced ICE technologies with clean energy sources to ensure engine stability while striving for carbon neutrality represents a prominent research hotspot [30–32].

Based on the above analysis, although rotational speed has been identified as a dominant factor governing CCV [23], the fundamental physical mechanisms, particularly how

speed-induced turbulence modifications interact with flame propagation to trigger end-gas auto-ignition, remain insufficiently understood. Conventional RANS models are limited in capturing these transient cyclic variations, while simplified chemistry models fail to accurately predict the complex ignition delay of knock. Therefore, the primary motivation of this study is to bridge this gap by employing a high-fidelity multi-physics framework: LES is utilized to resolve the unsteady turbulent flow structures; the G-equation model [33] is applied to track the turbulent flame front position precisely; and the SAGE [16] detailed chemistry solver is coupled to capture the auto-ignition characteristics of the end-gas. By integrating these methods, this research aims to reveal the intrinsic correlation mechanisms between engine speed, turbulence intensity, and combustion stability.

## 2. Engine Calculation Model and Experimental Setup

### *2.1. Turbulence and Combustion Simulation Models*

The simulation of turbulence in engine CFD typically relies on three models. These include Direct Numerical Simulation (DNS) and Reynolds-averaged Navier–Stokes (RANS) simulation. Large Eddy Simulation (LES) also serves as a key technique [16]. As mentioned in the introduction, LES has more advantages in simulating the CCV phenomenon of internal combustion engines. Therefore, this study uses LES to simulate the turbulence phenomenon in internal combustion engines.

The fundamental governing equations of fluids are the fundamental physical laws that describe their motion. In this study, the governing equations after filtering processing satisfy fundamental conservation laws. These include the conservation of mass. They also satisfy the conservation of momentum. Finally, they obey the conservation of energy. These equations can be expressed by Equations (1)–(3) as follows:

$$\frac{\partial \overline{u_i}}{\partial x_i} = 0 \tag{1}$$

$$\frac{\partial \overline{u_i}}{\partial t} + \frac{\partial \overline{u_i u_j}}{\partial x_j} = -\frac{1}{\rho}\frac{\partial p}{\partial x_i} + v\frac{\partial^2 \overline{u_i}}{\partial x_i \partial x_j} \tag{2}$$

$$\frac{\partial \overline{T}}{\partial t} + \frac{\partial \left(\overline{u_j}\overline{T}\right)}{\partial x_j} = \frac{v}{Pr}\frac{\partial^2 \overline{T}}{\partial x_i \partial x_j} - \frac{\partial q_j}{\partial x_i} \tag{3}$$

where $\overline{u_i}$ and $\overline{u_j}$ are the time-average velocity components after filtering processing, $\rho$ is the density of the fluid, $v$ is the dynamic viscosity of the fluid, $p$ is the pressure of the fluid, $\overline{T}$ is the temperature after filtering processing, $Pr$ is the Prandtl number, in addition, as well as $q_j$, which denotes the subgrid heat flow rate. The sub-grid model adopts the improved single-equation sub-grid model by Menon et al. [34], in which the expression of sub-grid-scale stress $\tau_{ij}$ is expressed as:

$$\frac{\partial k}{\partial t} + \overline{u_i}\frac{\partial k}{\partial x_i} = -\tau_{ij}\frac{\partial p}{\partial x_i} - \varepsilon + v\frac{\partial}{\partial x_i}\left(\frac{v_t}{\sigma_k}\frac{\partial k}{\partial x_i}\right) \tag{4}$$

$$k = \frac{1}{2}\left(\overline{u_i^2} - \overline{u_i}^2\right) \tag{5}$$

where $k$ is the kinetic energy of the subgrid, $\varepsilon$ represents the local energy dissipation rate per unit mass of fluid and $v_t$ represents the turbulent viscosity.

Combustion is a complex physicochemical process. Selecting an appropriate combustion model is crucial for the accuracy of combustion prediction [35]. In this research, the SAGE model and the G equation are coupled for the combustion model, where the G equation is used to simulate the turbulent-chemistry interaction (TCI) during the flame propagation process [16]. A reduced primary reference fuel (PRF) mechanism comprising 48 species and 152 reactions was adopted to achieve a compromise between chemical fidelity and computational cost. Specifically, the mechanism integrates Tanaka's pyrolysis

model [36] with Tsurushima's low-temperature kinetics [37], essential for capturing the two-stage ignition delay characteristic of knock. Numerically, the SAGE solver handles the stiffness of the chemical source terms using an implicit integration scheme augmented by an analytical Jacobian. To further accelerate the simulation, an adaptive zoning strategy was implemented to group cells with similar thermodynamic states for collective kinetic solving, thereby significantly reducing the CPU overhead without compromising accuracy.

### *2.2. Engine Simulation Model and Grid Density Selection*

The schematic diagram of the three-dimensional engine model used in this study is shown in Figure 1. To capture the parameter information of the engine, eight monitoring points were uniformly set in the cylinder wall area. The boundary conditions of the temperature parameters are shown in Table 1.

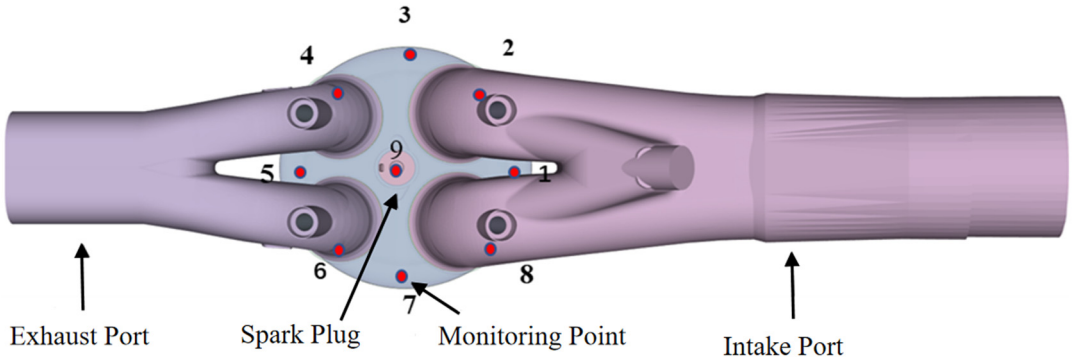



**Figure 1.** The schematic diagram of the three-dimensional engine model.

**Table 1.** Boundary conditions of temperature parameters.

| Boundary Conditions | Value |
|---|---|
| Piston | 450 K |
| Cylinder Head | 450 K |
| Cylinder Wall | 450 K |
| Intake Valve Underside | 480 K |
| Intake Valve Seat Angle | 480 K |
| Exhaust Valve Underside | 525 K |
| Exhaust Valve Seat Angle | 525 K |

In the CFD simulation of internal combustion engines, the selection of mesh density and the test of independence are key steps to obtain reliable calculation results [38]. Excessive grid density can improve the accuracy of simulation calculation, but it will bring unnecessary consumption of computing resources. Therefore, in order to study the CCV and detonation phenomena in internal combustion engines more accurately, while taking into account both calculation accuracy and calculation time, this study determines the minimum basic grid size based on three different grid sizes (2 mm, 1.4 mm, 2.6 mm). As shown in Figure 2, when the base mesh is set below 2 mm, the variation range of the cylinder pressure curve is relatively small. Therefore, the base mesh size of the model selected in this study is 2 mm.

The adaptive mesh refinement (AMR) strategy can achieve more precise resolution in the combustion process [16]. To obtain more detailed information on the flow field and scalar field within the internal combustion engine cylinder during the combustion process, this study uses the AMR strategy to perform separate mesh encryption on the regions with a large amplitude of variable changes within the cylinder. Three different strategies (speed, speed and temperature, speed and chemical reaction progress) were compared, as

shown in Figure 3. The adaptive grid encryption strategy based on temperature changes still increases the number of grids after the main combustion period, resulting in a waste of computing resources. After comprehensively considering the computing cost and accuracy, the AMR strategy based on speed and chemical reaction progress was selected. Some areas adopt a fixed embedding strategy. The encryption level and grid size parameters are shown in Table 2.

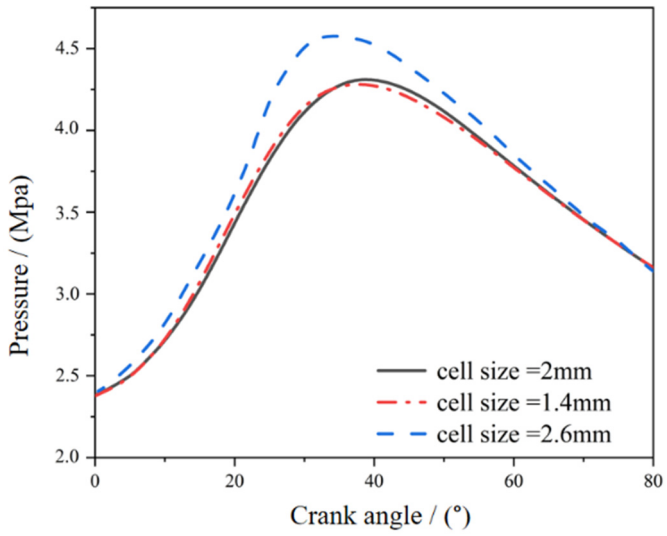



**Figure 2.** Grid independence test.

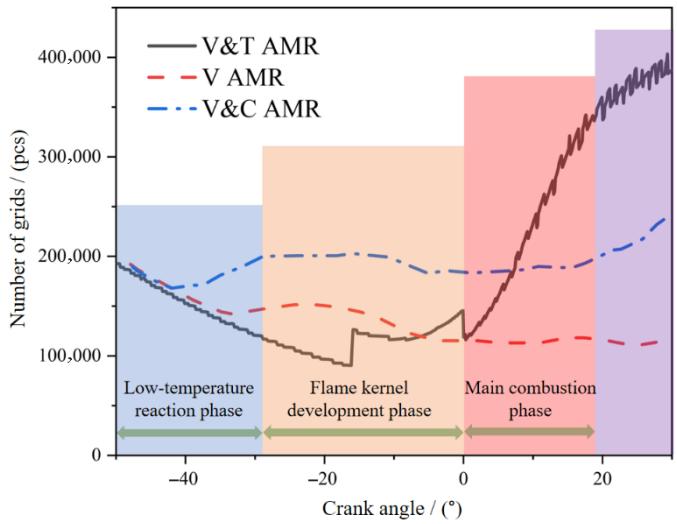



**Figure 3.** The comparison of different AMR strategies.

**Table 2.** The encryption level and grid size parameters.

| Fixed Embedding Area | Encryption Level | Grid Size/(mm) |
|---|---|---|
| Cylinder Wall | 1 | 1 |
| Intake Valve Seat Angle | 2 | 0.5 |
| Exhaust Valve Seat Angle | 1 | 1 |
| Spark Plug | 4 | 0.125 |
| Spark Plug Vicinity | 3 | 0.25 |

### *2.3. Verification of Numerical Models*

To verify the accuracy of the simulation calculation, an internal combustion engine bench as shown in Figure 4 was used, with the ignition advance Angle set at 17 CAD bTDC

and the intake passage pressure set at 0.1 Mpa. The bench test values were compared with the simulation values. The equipment and fuel information used are, respectively, presented in Tables 3 and 4. The engine speeds of 3000, 4000, and 5000 rpm were selected to represent the engine's characteristic operating conditions. Specifically, the 3000–4000 rpm range corresponds to the optimal operating window for fuel economy and power output, where knock mitigation is of primary concern. The 5000 rpm condition was included to further investigate the impact of high-speed turbulence on combustion stability and to extend the research scope to high-load limits.

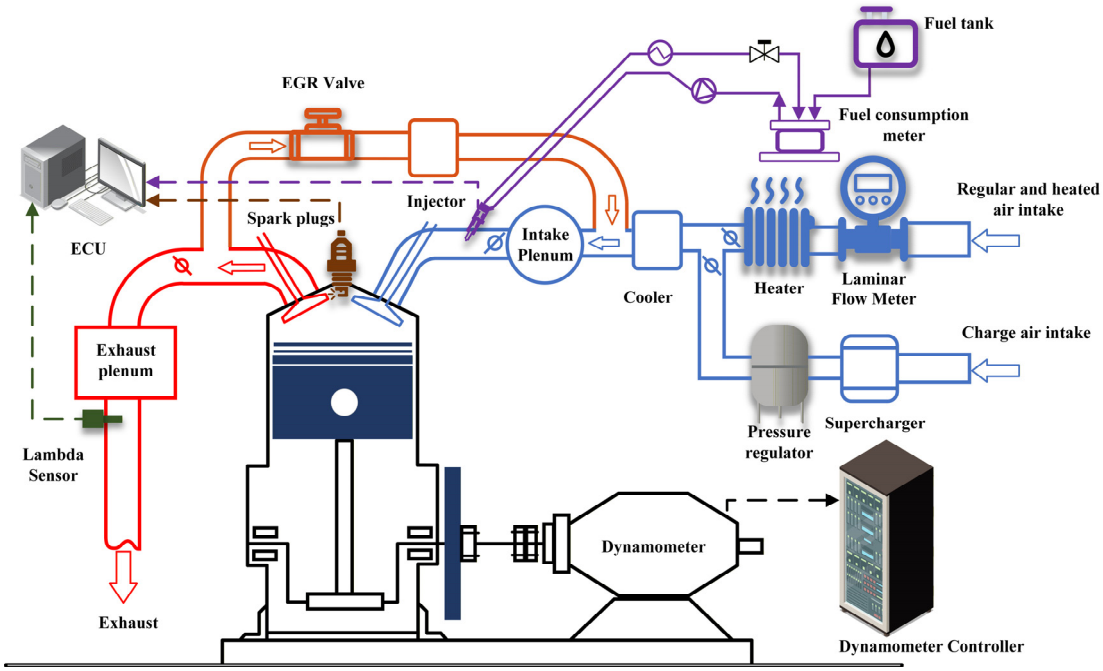



**Figure 4.** Schematic diagram of the engine test bench.

**Table 3.** Engine equipment information.

| Parameters | Value |
|---|---|
| Bore | 86 mm |
| Stroke | 90 mm |
| Compression ratio | 9.86 |
| Intake pressure | 0.1 Mpa |
| Excess air ratio | 1.0 |
| Ignition timing | 17 CAD bTDC |
| Rotational speed | 3000/4000/5000 (rpm) |
| Intake valve opening | −410 CAD aTDC |
| Intake valve closing | −100 CAD aTDC |
| Exhaust valve opening | 140 CAD aTDC |
| Exhaust valve closing | 370 CAD aTDC |

**Table 4.** Isooctane fuel information.

| Parameters | Value |
|---|---|
| Molecular formula | $C_8H_{18}$ |
| Octane number | 95 |
| Calorific value | 44.6 |
| Ignition point | 427 °C |

Figure 5a–c shows the comparison between the simulated and experimental values of the average pressure inside the cylinder under continuous working conditions of internal combustion engine combustion at three different rotational speeds (3000 rpm, 4000 rpm, 5000 rpm). As shown in the figure, the experimental and simulated in-cylinder pressure curves vary with the crankshaft angle, with closely matched combustion phases. It can be considered that the LES conducted in this study can well demonstrate the combustion process inside the cylinder. Table 5 summarizes the regression metrics comparing the simulated values with the experimental data. The results indicate that the simulation errors are minimal, and the model exhibits a high coefficient of determination ($R^2$), demonstrating strong goodness-of-fit. The simulation results have a certain degree of reliability.

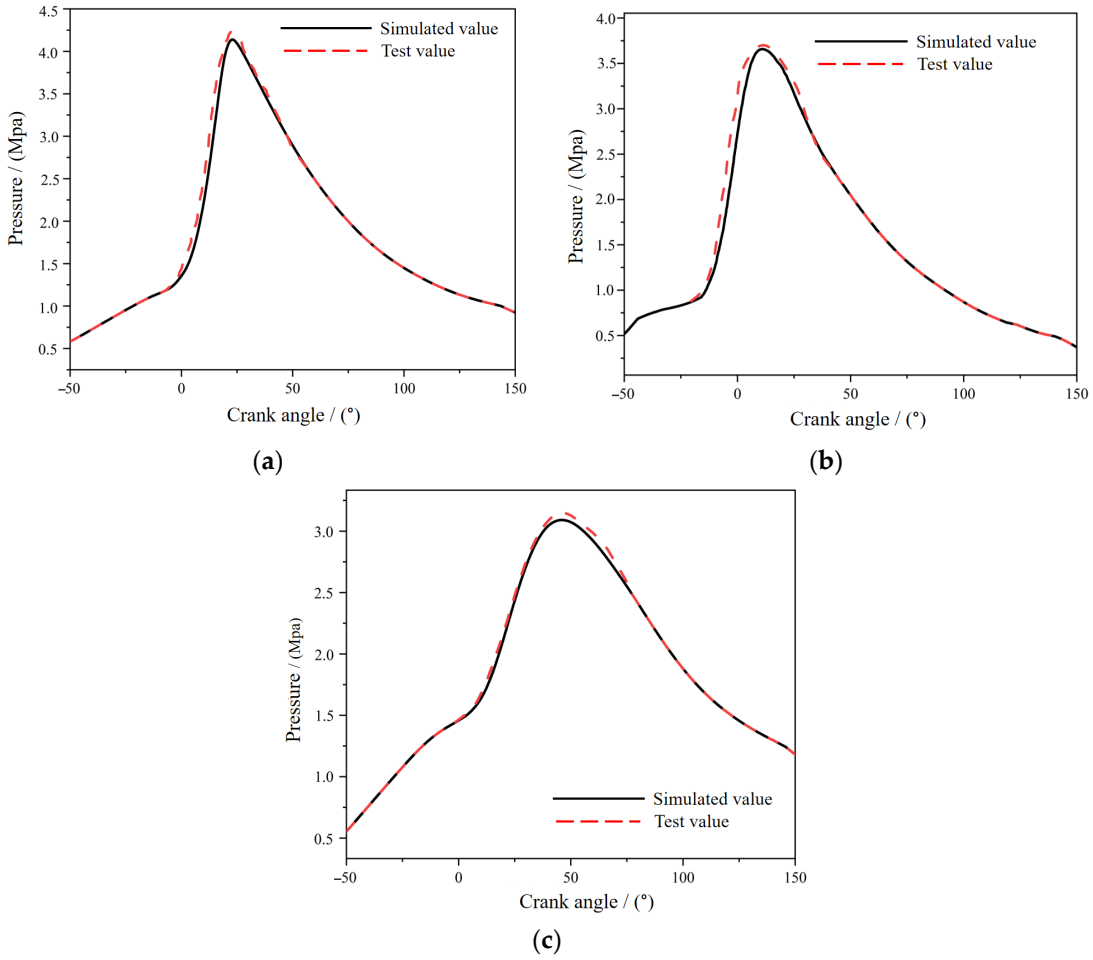



**Figure 5.** Comparison of simulated values and test values under different rotational speed conditions: (**a**) 3000 rpm, (**b**) 4000 rpm, (**c**) 5000 rpm.

**Table 5.** Regression metrics of the model.

| Speed Conditions | $R^2$ | RMSE | MAE | MAPE |
|---|---|---|---|---|
| 3000 rpm | 0.988 | 0.119 | 0.063 | 2.439 |
| 4000 rpm | 0.963 | 0.192 | 0.112 | 5.061 |
| 5000 rpm | 0.997 | 0.037 | 0.023 | 0.924 |
| Average | 0.983 | 0.116 | 0.066 | 2.808 |

## 3. Results and Discussion

### *3.1. The Effect of the Rotation Speed on the CCV*

To measure the CCV phenomenon in internal combustion engines, researchers generally use the variation curve of cylinder pressure with crankshaft rotation angle [23,39]. In this research, the maximum burst pressure and the crankshaft rotation Angle corresponding to the maximum pressure are adopted as evaluation indicators. The coefficient of variation (COV) of the maximum burst pressure refers to the calculation formula in the study by Azeem et al. [9]:

$$COV_P = \left(\frac{\sigma}{\mu}\right)_P \times 100\% \quad (6)$$

where $\mu$ and $\sigma$ are, respectively, the mean and standard deviation of the sample in statistics.

Correspondingly, the formula related to the cyclic fluctuation rate of the crankshaft angle corresponding to the peak average pressure in the cylinder is similar to the formula corresponding to the pressure, which is:

$$COV_\varphi = \left(\frac{\sigma}{\mu}\right)_\varphi \times 100\% \quad (7)$$

Since the rotational speed affects the maximum burst pressure of the engine, the definition of the burst pressure intensity cycle in this study is based on the relative values of the maximum burst pressure of the engine at different rotational speeds. The cycles with the lowest, highest and median values of the maximum burst pressure at each rotational speed are, respectively, taken as the characteristic cycles. Figure 6 shows the average pressure curves in different circulation cylinders of the internal combustion engine simulated in this study at three rotational speeds of 3000 rpm, 4000 rpm and 5000 rpm. The results show that the maximum burst pressure of the engine continuously increases with the increase in working cycles and fluctuates around the average value of the maximum pressure peak in the cylinder. In addition, the combustion phase also shows differences in multi-cycle simulations, especially in the 3000 rpm cycle, where this fluctuation is more obvious.

The cyclic volatility of the engine at different speeds is shown in Figure 7. When the engine speed is within the range of this study, the $COV_P$ of the maximum burst pressure reaches the peak at 14.9% at 3000 rpm, showing a drop to 11% at 4000 rpm. Additionally, as the speed continues to increase, $COV_P$ further declined to a minimum of 9.48%, indicating that within the range of rotational speed research, as the rotational speed increases, the cyclic volatility of the maximum burst pressure of the internal combustion engine continuously decreases, suggesting that the combustion of the internal combustion engine tends to stabilize. However, the corresponding cyclic fluctuation rate of the crankshaft Angle is not consistent with it. Although $COV_\varphi$ reaches the maximum value of 7.8% at 3000 rpm and drops to 6.8% when the rotational speed increases to 4000 rpm, when the rotational speed continues to increase to 5000 rpm, $COV_\varphi$ rises to 8.1%. It is indicated that when the engine speed is 5000/min, the propagation speed of the main flame in the cylinder has a strong cyclic fluctuation characteristic. This might be because an increase in rotational speed continuously intensifies the turbulence intensity within the cylinder, making the turbulent combustion during flame propagation more thorough. However, when the rotational speed is too high, the turbulence may become overly chaotic, leading to unstable flame propagation [40]. In addition, at high rotational speeds, the strong turbulence level inside the cylinder will increase the energy release during the formation of the fire nucleus and the small-scale spherical flame expansion stage, increasing the instability of the early flame propagation speed and affecting the maximum pressure increase rate [41], which in turn leads to an increase in the cyclic fluctuation rate of the crankshaft angle corresponding to the maximum burst pressure of the engine.

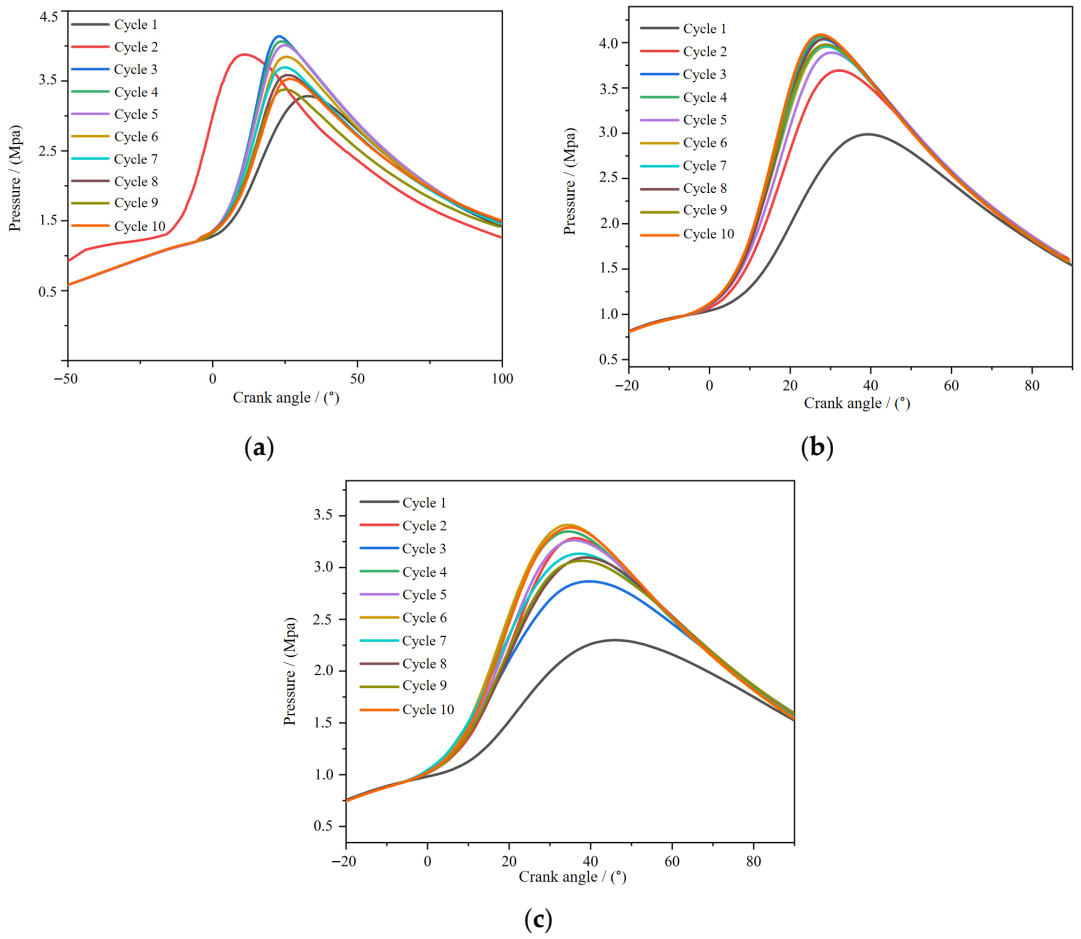



**Figure 6.** The average pressure curves in different circulation cylinders of the engine at different rotational speeds: (**a**) 3000 rpm, (**b**) 4000 rpm, (**c**) 5000 rpm.

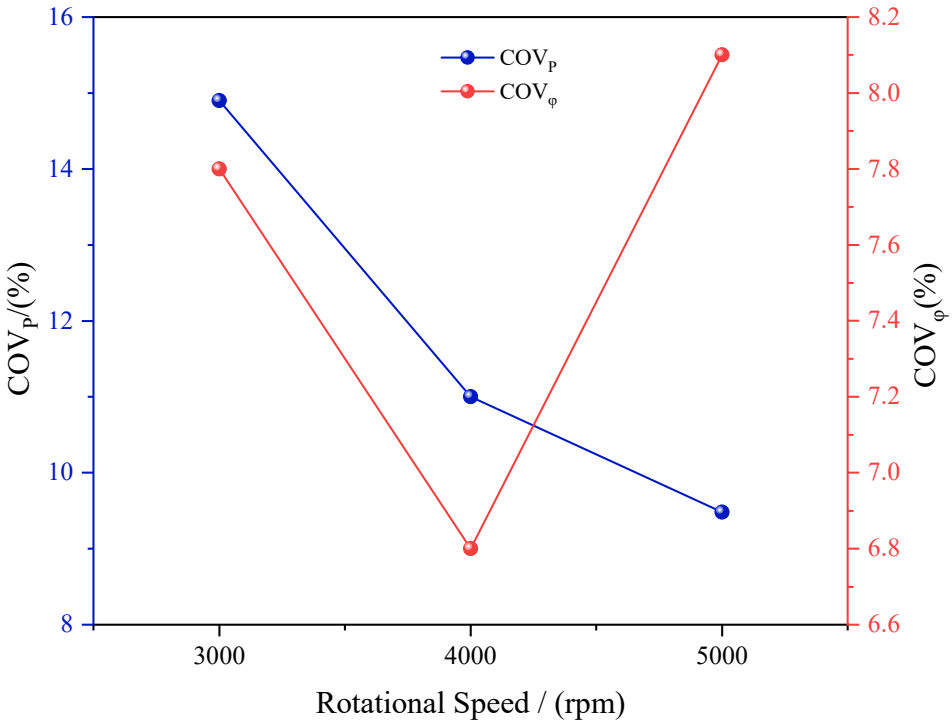
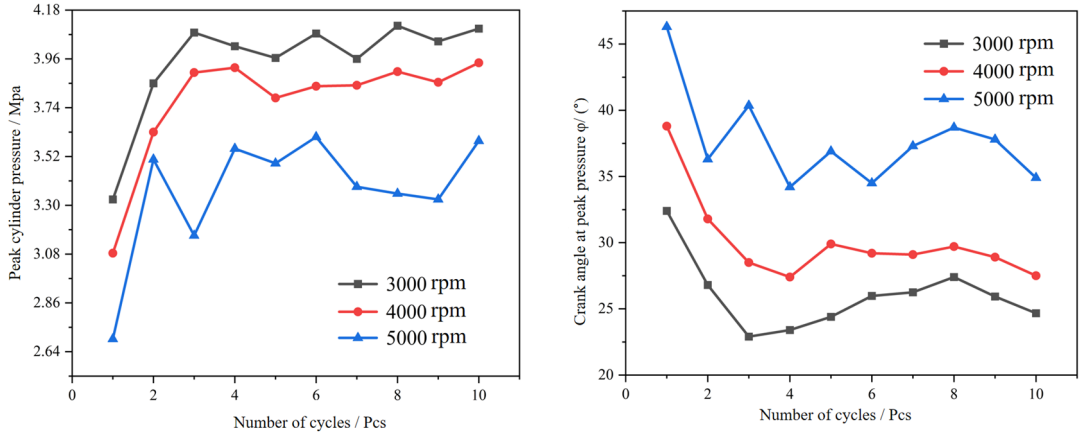



**Figure 7.** The cyclic fluctuation phenomenon of the engine at different rotational speeds.

Figure 8 illustrates the maximum in-cylinder pressure and the corresponding crank angle for each cycle under different engine speeds. This graph visually depicts the variation trends of both the maximum pressure and its associated crank angle as the number of working cycles increases. Analysis of the crank angle corresponding to the maximum pressure reveals a consistent pattern across different speeds: the first cycle exhibits a relatively large crank angle, which then decreases rapidly with subsequent cycles and eventually fluctuates around a certain level. This phenomenon occurs because, during the first cycle, the in-cylinder scalar and flow fields are in their initial states, characterized by low temperature and weak flow intensity, resulting in a slower turbulent flame propagation speed. Consequently, a larger crank angle is required to reach the peak pressure. Moreover, as the engine speed increases, the crank angle corresponding to the maximum pressure also increases. This is due to the reduced flame propagation distance per degree of crank angle at higher speeds. Additionally, the maximum in-cylinder pressure under each speed condition gradually rises with an increasing number of cycles. Within the speed range of 3000 to 5000 rpm, an increase in engine speed leads to a reduction in the peak cylinder pressure.




(**a**) (**b**)

**Figure 8.** The variation in the maximum burst pressure at different rotational speeds and the corresponding crankshaft rotation angle with the number of cycles: (**a**) the maximum burst pressure, (**b**) the corresponding crankshaft rotation angle.

The above results indicate that as the rotational speed of the internal combustion engine continuously increases, its maximum burst pressure and the corresponding crankshaft rotation Angle show inconsistent variation patterns. However, to analyze the causes and dynamic mechanisms of this phenomenon, it is necessary to conduct separate analyses from the scalar field and vector field of combustion in the cylinder.

### *3.2. Static Inducement of CCV in Internal Combustion Engines*

CCV in engines is primarily caused by initial differences in the in-cylinder scalar field at ignition. It is also caused by cyclic fluctuations in this field. These variations affect key factors such as the mixture state. They also impact the turbulence field and the fuel distribution. At the same time, in-cylinder temperature also affects combustion stability by influencing fuel evaporation and mixture quality [41,42]. Figure 9 presents cross-sectional views of the temperature distribution under different peak pressure cycles across a range of engine speeds, from 3000 to 5000 rpm. The data was captured at 20 CAD bTDC. The results indicate that as the engine speed increases, the in-cylinder initial temperature also rises. This trend is attributed to enhanced turbulent combustion and greater heat release at higher speeds. However, the accumulated heat is not dissipated efficiently, leading

to an expansion of high-temperature regions under high-speed conditions. Notably, no definitive correlation is observed between the initial temperature and the peak firing pressure intensity. In cycles with lower peak pressure, the high-temperature zone is more extensive. Under the same speed condition, the initial temperature distributions among cycles with medium to high peak firing pressure exhibit only minor variations, suggesting that temperature is not the primary factor contributing to cyclic variations. Furthermore, as engine speed increases, the temperature distribution within the cylinder becomes more heterogeneous. The temperature near the wall rises progressively, which increases the likelihood of end-gas auto-ignition and thereby elevates the propensity for engine knock. The results indicate that as the engine speed increases, the in-cylinder initial temperature also rises. It should be noted that although the boundary wall temperatures are fixed at 450–525 K (as listed in Table 1), the bulk gas temperature at this timing (20 CAD bTDC) is significantly higher due to the compression work performed by the piston. The numerical model accounts for this steep temperature gradient near the boundaries using a wall heat transfer function to calculate the heat loss from the hot gas to the cooler cylinder walls.

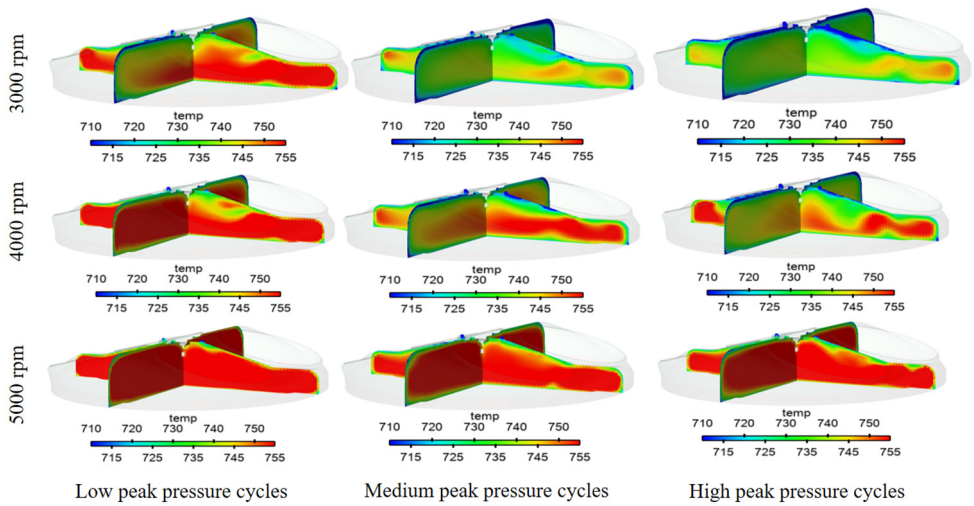



**Figure 9.** The temperature distribution inside the cylinder under three different rotational speed conditions and detonation cycles at 20 CAD bTDC.

Figure 10 presents cross-sectional views of the residual gas distribution (represented by a 1% $CO_2$ concentration) under different engine speeds and different peak pressure cycles at the 20 CAD bTDC. $CO_2$, a primary product of combustion, is used here as a tracer. Furthermore, its distribution reflects the distribution of other residual gas components, such as particulate matter. These particles can act as potential hot spots, potentially triggering auto-ignition of the end-gas during the high-pressure combustion phase and increasing knock propensity. The results indicate that the 1% $CO_2$ concentration zone is predominantly located near the intake valve side of the combustion chamber wall within the rotational speed range of this study. This distribution pattern arises because the flow field intensity near the closed intake valve is relatively low during the exhaust stroke. Furthermore, during the subsequent intake stroke, the gas near the intake valve wall is less influenced by the fresh charge jet, resulting in limited turbulent mixing of the residual gas with the incoming air-fuel mixture. As engine speed increases, the area of the 1% $CO_2$ concentration zone decreases significantly. This reduction is attributed to enhanced gas exchange efficiency and increased volumetric airflow at higher speeds, which improves the scavenging of residual gases from the cylinder. Furthermore, cycles with higher peak firing pressure exhibit a more extensive 1% $CO_2$ concentration zone at the time of ignition. This correlation can be explained by the higher temperature of the residual gas relative to the fresh mixture. The

presence of this warmer residual gas promotes the chemical reaction rate during the main combustion event, leading to a higher peak pressure.

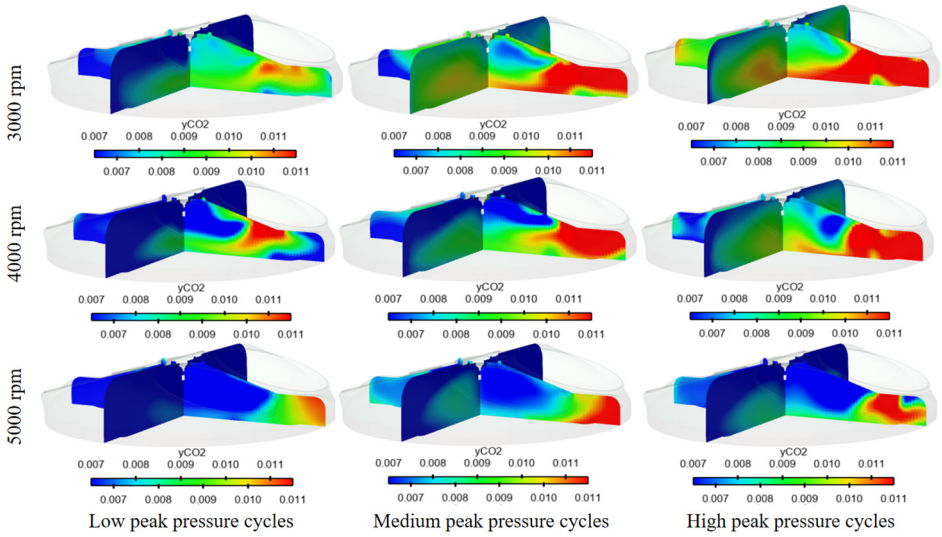



**Figure 10.** The exhaust gas distribution inside the cylinder under three different rotational speed conditions and detonation cycles at 20 CAD bTDC.

Figure 11 illustrates the fuel concentration distribution under different engine speeds and peak firing pressure cycles. The results indicate that at high speeds, fuel-rich zones prone to auto-ignition are concentrated near the intake valve side, whereas at low speeds, these zones are primarily located at the bottom of the combustion chamber. As the engine speed increases, the intensified intake airflow leads to a leaner fuel-air mixture in the central region of the cylinder. This leanness in the core region is a contributing factor to the observed decrease in the peak firing pressure with increasing speed. Furthermore, higher engine speeds result in a steeper fuel concentration gradient along the path from the spark plug to the intake valve side. This inhomogeneity in mixture distribution causes an uneven combustion reaction rate of the main flame front, which in turn intensifies the cyclic variation in the crank angle corresponding to the peak firing pressure.

To further verify the occurrence of auto-ignition inferred from the scalar fields, the heat release rate (HRR) evolution was analyzed. Figure 12 compares the HRR profiles of cycles with different knock intensities. It can be observed that the high-knock cycle exhibits a characteristic two-stage heat release pattern. Following the primary combustion phase driven by the flame propagation, a sharp, high-amplitude spike in heat release occurs such as around 10° ATDC. This sudden spike signifies the instantaneous volumetric combustion of the end-gas pockets, which releases energy at a rate significantly higher than the normal flame front. This dynamic signature provides robust evidence that the fuel-rich, high-temperature regions identified in Figures 9–11 indeed evolved into auto-ignition centers, leading to knock.

### *3.3. The Dynamic Mechanism of CCV in Internal Combustion Engines*

Turbulent combustion is a key factor influencing the flame propagation speed [43]. Turbulence not only alters the macroscopic form of the flame but also directly affects its microscopic chemical reaction process, ultimately significantly increasing the flame propagation speed [44]. The turbulent motion state within the cylinder not only determines the turbulent transport effect but also influences the distribution of fuel at the end. It also has a crucial impact on the speed of flame propagation [45]. Turbulent kinetic energy is the average value of the pulsating kinetic energy of fluid turbulence, representing the

intensity of turbulent motion and can be used to measure the performance of internal combustion engines [46,47]. The turbulent kinetic energy of an internal combustion engine has a strong relationship with the intake valve and rotational speed, generally increasing with the increase in rotational speed [48]. As shown in Figure 13, it is the variation curve of the turbulent kinetic energy of an internal combustion engine with rotational speed in this research.

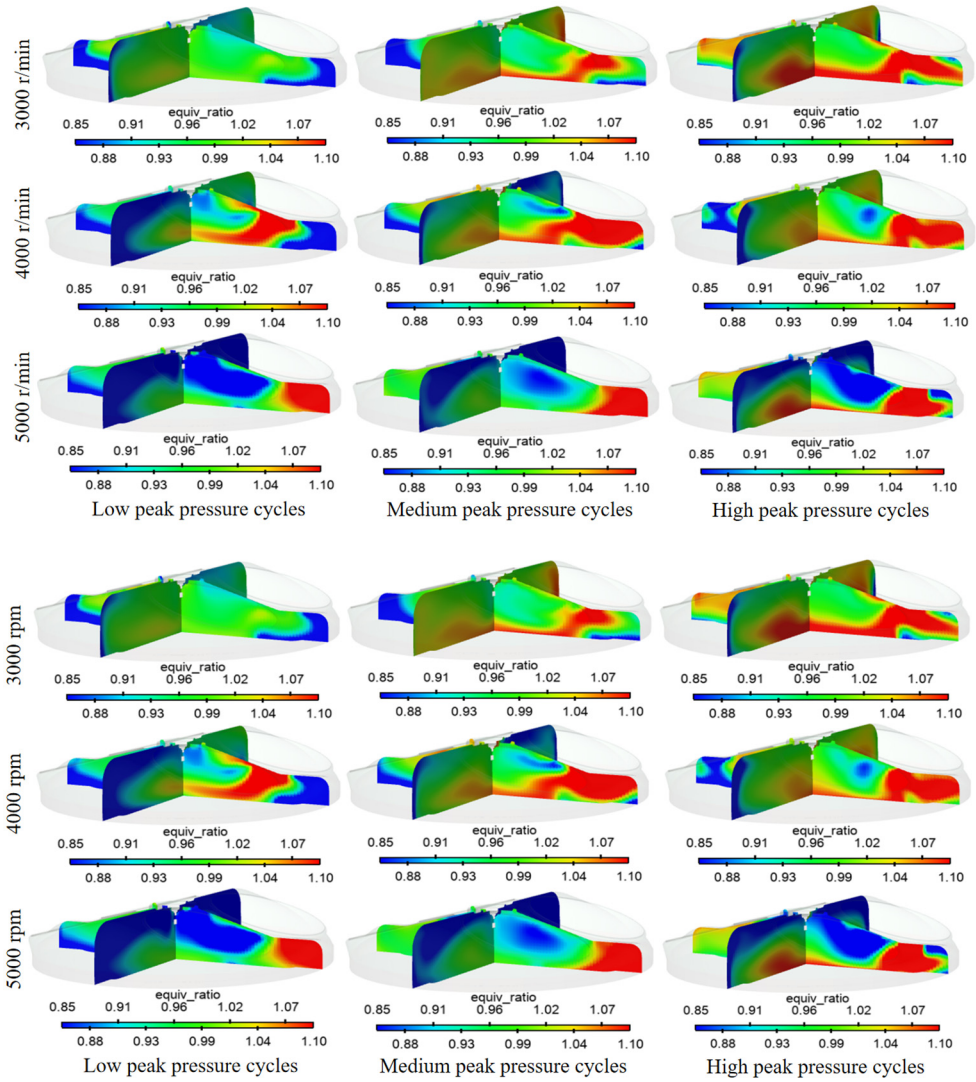



**Figure 11.** The fuel distribution inside the cylinder under three different rotational speed conditions and detonation cycles at 20 CAD bTDC. Note: The color bar represents mass fraction values (e.g., 0.01 corresponds to 1%).

The in-cylinder flow field exhibits cyclic variations. High-speed jets generate significant turbulent kinetic energy within the combustion chamber, thereby enhancing the mixing of the jet with the surrounding mixture [49]. As a result of the intake jet's influence, a large-scale vortex structure forms in the region between the intake and exhaust valves, as illustrated in Figure 14. The black vector arrows denote the fluid flow direction. The underlying color contour represents the velocity magnitude (in m/s), where dark blue regions indicate low-velocity zones. The variations in arrow magnitude and color directly indicate the level of mean TKE. It can be observed that large-scale vortices are symmetrically distributed on both sides of the horizontal axis between the exhaust and intake valves. Near the intake valve wall, the flow moves downward from the cylinder head toward the piston, imparting a momentum that transports the fresh mixture toward the piston bottom.

However, large-scale vortices are relatively inefficient at transporting a significant mass of fuel-air mixture. This inefficiency results in a pronounced fuel concentration gradient from the spark plug to the intake valve side, consequently exacerbating the CVC.

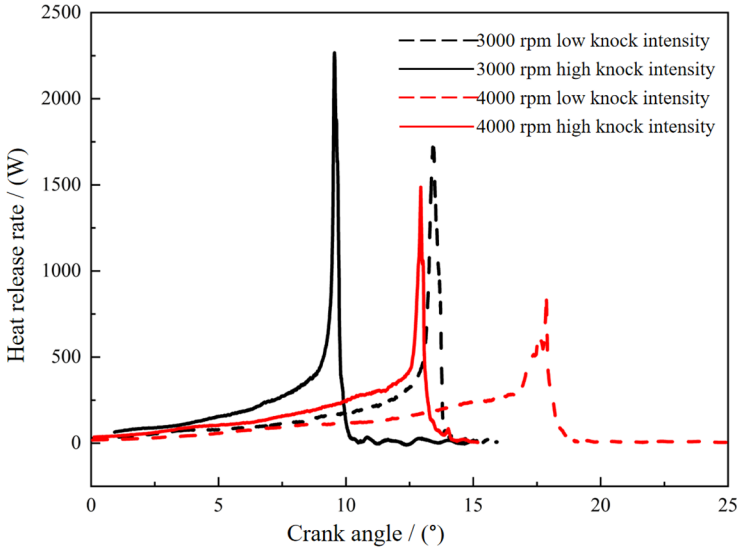



**Figure 12.** Heat release rate curves between low-knock and high-knock cycles at 3000 and 4000 rpm.

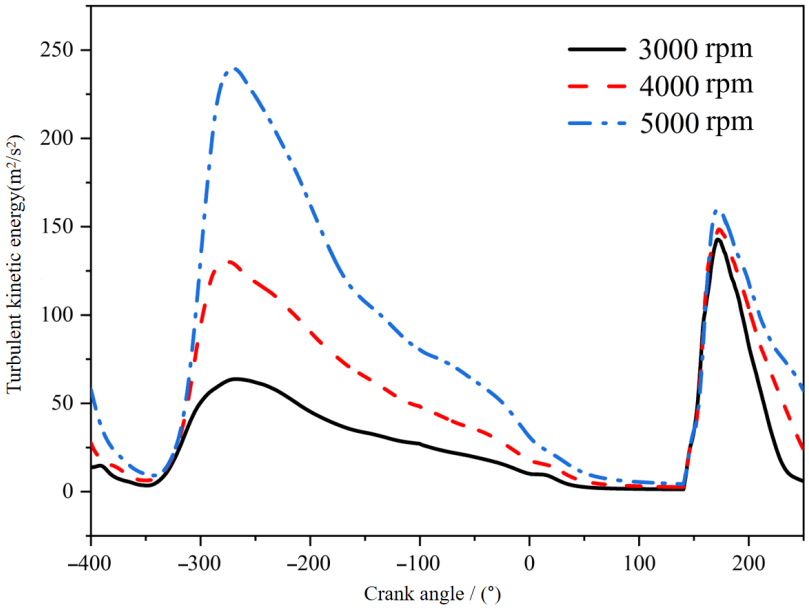



**Figure 13.** The curve of turbulent kinetic energy varies with crankshaft rotation angle and rotational speed.

Figure 15 shows the intensity of the flow field distributions under different conditions. Note that the solid black circle marks the physical location of the spark plug electrode; as a solid boundary, the velocity within this region is zero. Surrounding dark regions indicate low-velocity stagnation zones formed in the wake of the spark plug geometry. The high-turbulence field is distributed roughly symmetrically about the horizontal axis between the exhaust and intake valves. Furthermore, its intensity increases with engine speed. During the main flame propagation phase, the flame front propagates faster vertically due to a higher turbulent burning rate in that direction, while its horizontal development is slower. Consequently, when the pressure from the main flame significantly compresses the end-gas region, a large area of unburned mixture near the intake valve remains highly susceptible to auto-ignition. Secondly, in high-pressure cycles, the stronger

turbulence near the spark plug promotes the early expansion of small-scale spherical flames, which accelerates subsequent flame propagation and ultimately leads to a higher peak in-cylinder pressure.

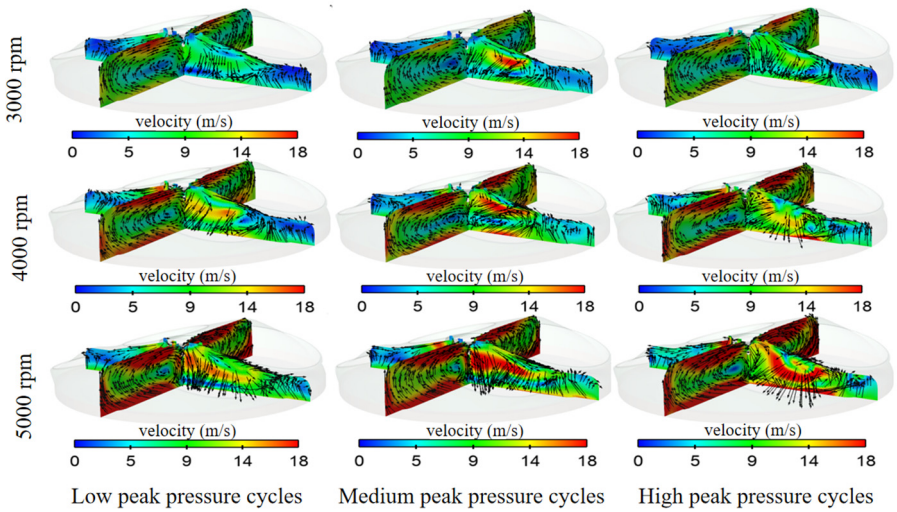



**Figure 14.** The flow field distribution inside the cylinder under three different rotational speed conditions and detonation cycles (velocity in m/s).

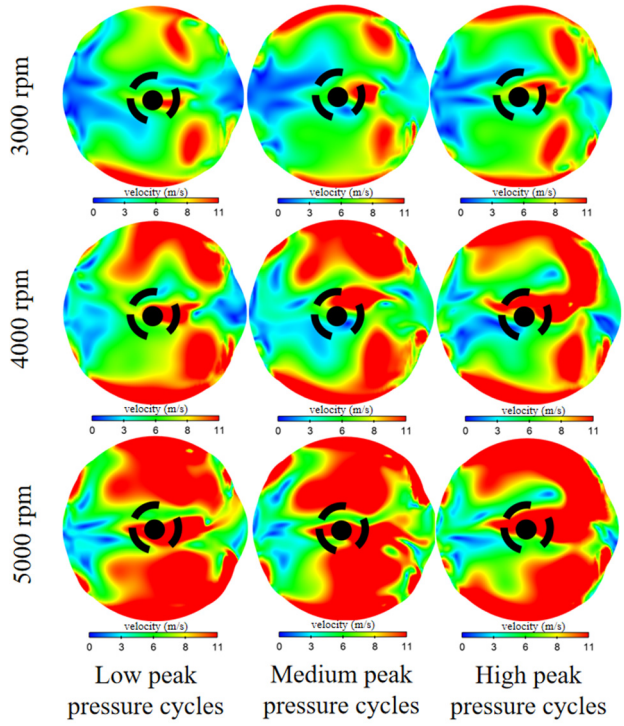



**Figure 15.** The intensity of the flow field below at 20 CAD bTDC. (Note: Different velocity scales are used in Figures 14 and 15 to highlight the specific local flow structures, velocity in m/s).

### *3.4. Discussion*

The combustion stability is governed by the competition between two critical parameters identified in this study: in-cylinder turbulence intensity (stabilizing factor) and mixture homogeneity (destabilizing factor). The dominant effect of increasing engine speed is the significant amplification of TKE, as shown in Figure 13. This enhanced turbulence stabilizes the early flame kernel development, making it more robust against stochastic variations. Consequently, the peak pressure fluctuation shows a continuous reduction (from 14.9% to

9.48%), indicating a consistent improvement in the stability of the energy release magnitude. However, at the highest speed (5000 rpm), the reduced time available for mixing creates steeper fuel concentration gradients. This inhomogeneity begins to outweigh the benefits of turbulence for flame timing, causing the variability of the corresponding crank angle to rebound (rising from 6.8% to 8.1%). Therefore, comparing these parameters reveals a trade-off: while higher engine speed improves the amplitude stability due to enhanced turbulence, it introduces slight instability in the combustion phasing at very high speeds due to poorer mixture homogeneity.

To quantitatively investigate the CCV under different engine speeds and peak pressure conditions, the CA50 (the crank angle at which 50% of the fuel mass has been burned) was employed in this study to quantify the main combustion phase and flame propagation speed. Figure 16 shows the variation curve of fuel mass consumption of the engine with crankshaft rotation Angle under different rotational speeds. The results indicate that a significant difference in engine fuel consumption occurs around 10 CAD. This peak difference in fuel mass evolutions across cycles is also shown to increase with rotational speed. Specifically, the fastest fuel depletion is observed at 3000 rpm, with the 50% fuel mass fraction point occurring at 15 CAD. When the rotational speed is increased to 4000 rpm, the 50% fuel mass fraction point is delayed to 19 CAD. When the rotational speed is 5000 rpm, the 50% fuel mass fraction point of the engine is delayed to 22 CAD. Obviously, an increase in engine speed will reduce the fuel consumption process, which indicates that an increase in speed will decrease the propagation speed of the main flame during the crankshaft rotation Angle time. Under normal circumstances, an increase in rotational speed will enhance the flow field intensity within the cylinder, thereby increasing the flow combustion rate of the main flame in real time. However, when the crankshaft rotation time is taken as a reference, the propagation speed of the main flame decreases with the increase in rotational speed. This is because at higher rotational speeds, although the flow field velocity within the cylinder increases, the increase in flame propagation speed caused by enhanced turbulence cannot compensate for the delay effect of flame propagation within the crankshaft rotation Angle time resulting from the increase in rotational speed. The retardation of CA50 at high engine speeds can be physically interpreted through a scaling argument comparing physical time (ms) and crank angle domain (CAD). As the engine speed increases, the turbulent kinetic energy and intensity increase quasi-linearly, leading to a higher turbulent flame speed in the physical frame. However, the physical time available for the flame to propagate per crank angle degree decreases inversely with speed. Ideally, for the combustion phasing (CA50) to remain constant in the CAD, the flame speed must increase proportionally to the speed. However, the turbulent flame speed is a function of both turbulence and laminar flame speed. Since the chemical timescale governed by the laminar flame speed is primarily dependent on thermodynamic state rather than flow speed, the overall increase in turbulent flame speed is insufficient to fully offset the drastic reduction in the physical time available for the flame to propagate per crank angle degree at high rpms. Consequently, although the combustion process accelerates in terms of milliseconds, it effectively slows down relative to the angular motion of the crankshaft, resulting in the observed delay in CA50. When the rotational speed is constant, the propagation speed of the main flame is positively correlated with the maximum burst pressure of the engine. Figure 17 shows the fuel consumption curves under the same rotational speed but different detonation pressure cycles. The results in the figure indicate that high detonation pressure cycles usually achieve better fuel economy. This is because the turbulence in high detonation pressure cycles is relatively stronger, which enables more thorough gas mixing, thereby resulting in faster and more complete combustion and higher power efficiency of the internal combustion engine [50].

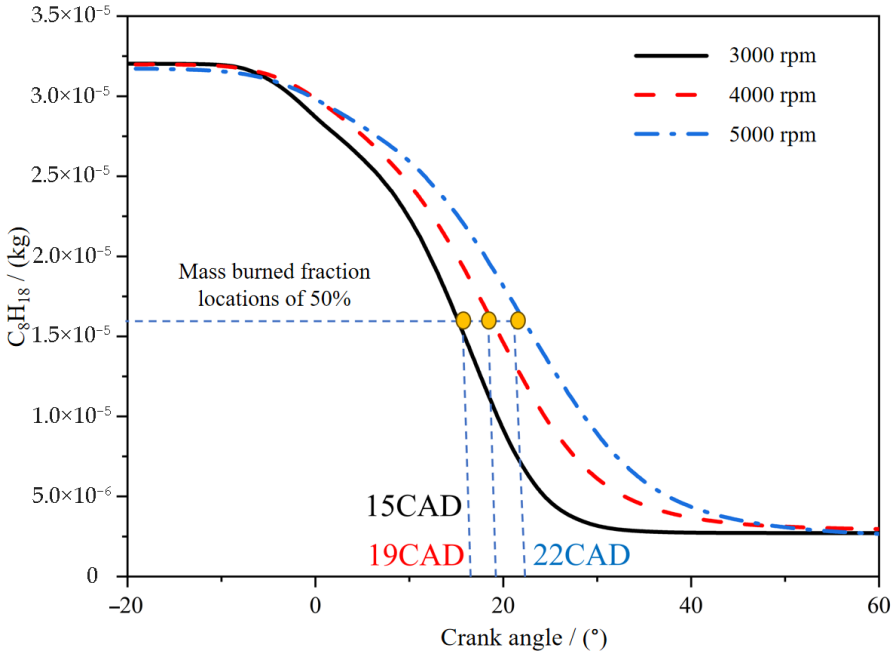



**Figure 16.** Evolution of in-cylinder fuel mass under different engine speeds.

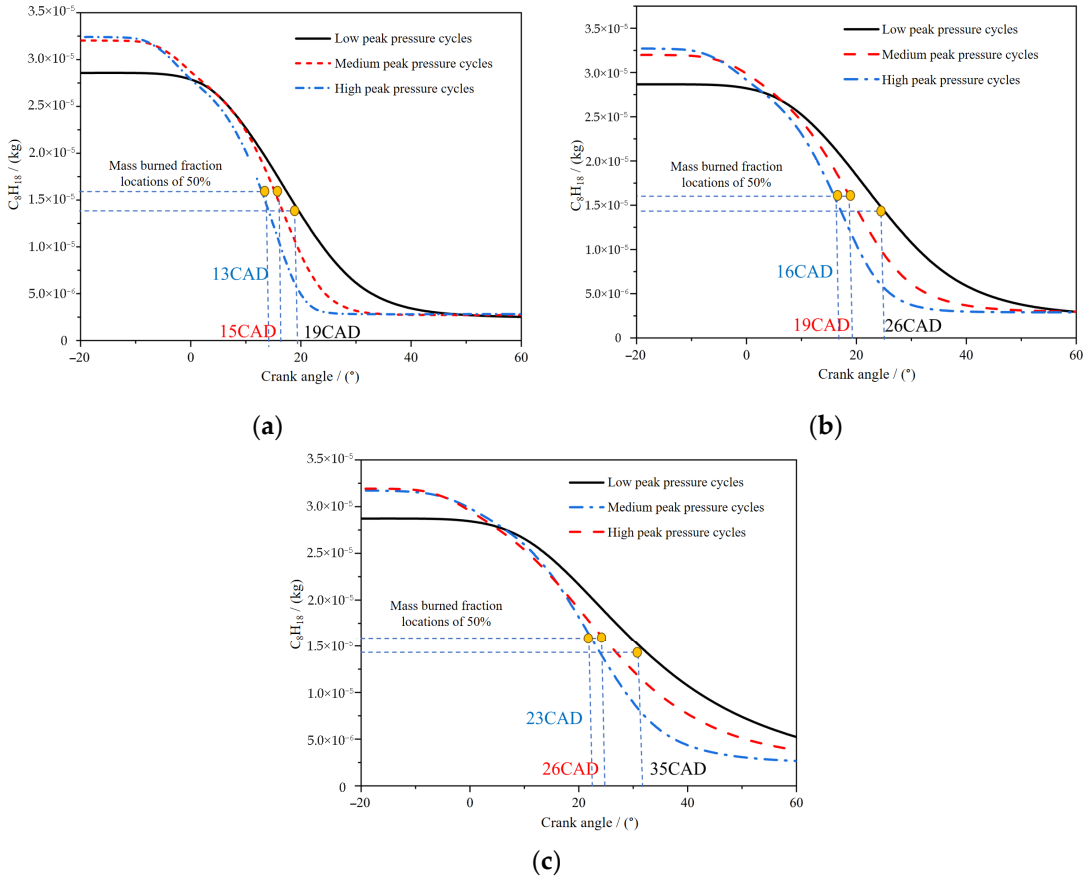



**Figure 17.** Fuel consumption curves under the same rotational speed but different detonation cycles: (**a**) 3000 rpm, (**b**) 4000 rpm, (**c**) 5000 rpm.

Figures 18 and 19 illustrate the development process of flame kernel formation and subsequent expansion in low peak pressure and high peak pressure cycles, respectively, under different engine speeds. Comparing the texture and contour of the flame propagation fronts at different speeds reveals that an increase in rotational speed results in a smaller

main flame front area at the same crank angle. During the initial formation stage, the flame kernel exhibits a near-spherical morphology. However, influenced by the turbulent flow distribution near the spark plug, the flame front already shows slight wrinkling by 5 CAD bTDC, with a larger geometric extent in the horizontal direction. This occurs because the flow field near the spark plug at the moment of ignition affects the flame surface morphology, which in turn influences subsequent flame propagation speed and the degree of wrinkling. The strong turbulent flow field near the spark plug is distributed predominantly along the horizontal direction, causing the flame front propagation speed in the weak-turbulence direction to lag behind that in the strong-turbulence direction.

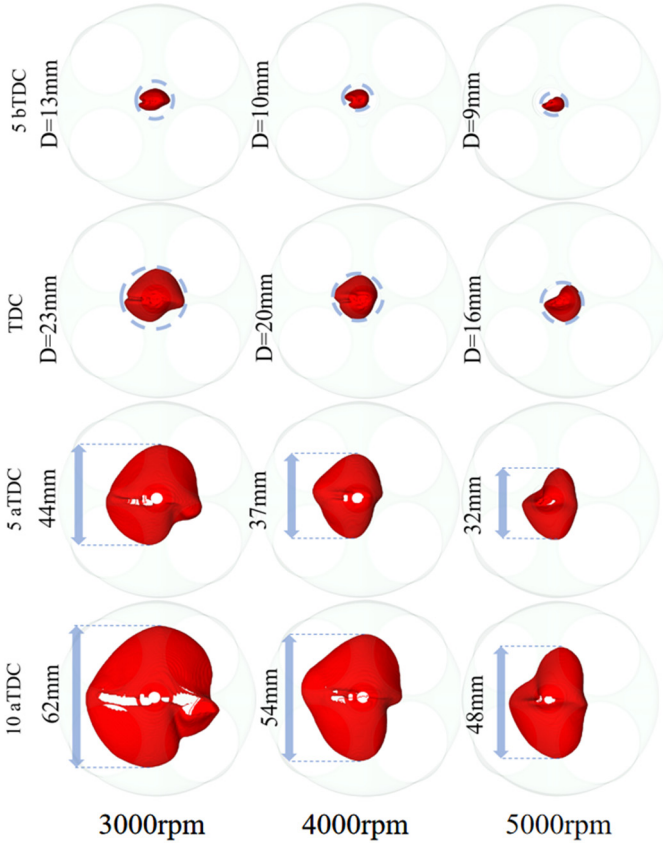



**Figure 18.** The flame kernel development process of low peak pressure cycles under three different rotational speed conditions.

As the flame front develops further, combustion transitions gradually from laminar to turbulent. Due to the symmetric distribution of large-scale vortices along the horizontal central axis in the initial flow field, the main flame propagates faster in the vertical direction than in the horizontal direction during the period from piston top dead center to 10 CAD aTDC. This leads to a flame front whose vertical dimension exceeds its horizontal dimension. When the main flame approaches the end of the combustion phase (around 10 CAD aTDC), the flame front sizes under different speeds show significant differences. Specifically, at 3000 rpm, the major axis length of the main flame front reaches 62 mm, whereas at 5000 rpm, it is only 48 mm at the same crank angle.

In the early stage of flame development, when the flame kernel is in a quasi-spherical phase (from 5 CAD bTDC to the Top Dead Center), the flame front develops fastest at 3000 rpm and slowest at 5000 rpm, indicating that the early development state of the flame kernel determines the subsequent main flame propagation speed. Due to the similarity in the geometric morphology of the main flame front during the development phase across different engine speeds—where the flame propagates faster vertically and slower

horizontally from the exhaust valve to the intake valve—by the end of the main flame development phase, the flame approaches the cylinder wall along its major axis, while a significant volume of unburned mixture remains near the intake valve side along the minor axis. At this point, the flame exerts strong compression on the end-gas mixture in this region. Under the combined effect of high temperature and high pressure, the area near the intake valve wall is highly prone to end-gas auto-ignition, leading to engine knock.

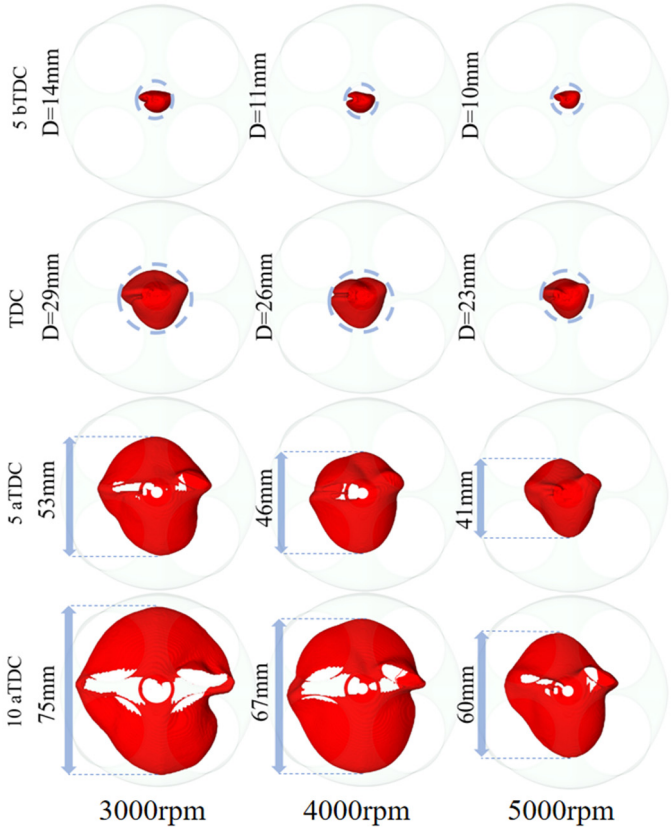



**Figure 19.** The flame kernel development process of high peak pressure cycles under three different rotational speed conditions.

## 4. Conclusions

This study investigated the mechanisms of CCV and end-gas auto-ignition under varying engine speeds using LES coupled with the G-equation and SAGE chemistry models. The key findings are summarized as follows:

(1) CCV Characteristics: Increasing engine speed monotonically reduces the fluctuation of the maximum burst pressure (the maximum of $COV_P$ decreased from 14.9% to 9.48%). In contrast, the $COV_\varphi$ exhibits a non-monotonic trend (first decreasing, then increasing). Additionally, a strong negative correlation was observed between the peak pressure and its corresponding crank angle.

(2) Effect of Initial Conditions: High peak pressure cycles are correlated with broader distributions of hot residual gas at ignition, which accelerates the early chemical reaction rate. Conversely, higher engine speeds steepen the fuel concentration gradient from the spark plug to the intake valve. This inhomogeneity in the mixture amplifies the cyclic variability of the combustion phasing.

(3) Turbulence and Flame Propagation: Enhanced turbulence at high speeds promotes early flame kernel development; however, it is insufficient to fully compensate for the reduced physical time per crank angle, resulting in retarded combustion phasing (CA50 delayed from 15 to 22 CAD). Furthermore, the symmetric flow structure directs

the flame front evolution, making the intake valve region the primary site for end-gas auto-ignition (knock).

**Author Contributions:** Validation, M.C. and M.L.; Formal analysis, M.C.; Data curation, M.P.; Writing—original draft, Z.Z.; Writing—review & editing, Z.Z.; Supervision, M.P., W.G. and H.S.; Funding acquisition, H.W., S.Z. (Shengkai Zhou), S.Z. (Song Zhang) and H.S.; Visualization, H.W., S.Z. (Shengkai Zhou), S.Z. (Song Zhang) and M.L.; Project administration, Z.Z. and H.S.; Software, W.G. All authors have read and agreed to the published version of the manuscript.

**Funding:** This research was funded by Guangxi Natural Science Foundation [2022GXNSFFA035029], Guangxi Science and Technology Major Program [AA24206058] and this work was also supported by the Guangxi Bagui Young Scholars Project.

**Data Availability Statement:** The raw data supporting the conclusions of this article will be made available by the authors on request.

**Conflicts of Interest:** Authors Hui Wang, Shengkai Zhou, Song Zhang and Hailang Sang were employed by the company Guangxi Yuchai Machinery Group Co., Ltd. The remaining authors declare that the research was conducted in the absence of any commercial or financial relationships that could be construed as a potential conflict of interest.

## References

1. Agarwal, A.K.; Mounaïm-Rousselle, C.; Brequigny, P.; Dhar, A.; Hespel, C.; Patel, C.; Srivastava, D.K.; Duraisamy, G.; Le Moyne, L.; Sharma, N.; et al. Future of internal combustion engines using sustainable, scalable, and storable E-fuels and biofuels for decarbonizing transport and enabling advanced combustion technologies. *Prog. Energy Combust. Sci.* **2025**, *110*, 101236. [CrossRef]
2. Song, C.H.; Jan Aaldering, L. Strategic intentions to the diffusion of electric mobility paradigm: The case of internal combustion engine vehicle. *J. Clean. Prod.* **2019**, *230*, 898–909. [CrossRef]
3. Priyam, A. Hydrogen as an alternative fuel for internal combustion engines: A review. *Sustain. Energy Technol. Assess.* **2025**, *82*, 104551. [CrossRef]
4. Vasan, V.; Sridharan, N.V.; Feroskhan, M.; Vaithiyanathan, S.; Subramanian, B.; Tsai, P.-C.; Lin, Y.-C.; Lay, C.-H.; Wang, C.-T.; Ponnusamy, V.K. Biogas production and its utilization in internal combustion engines—A review. *Process Saf. Environ. Prot.* **2024**, *186*, 518–539. [CrossRef]
5. Xu, S.; Hong, C.; Wang, S.; Qiang, Y.; Zhao, S.; Xiang, J.; Yang, J.; Ji, C. Research on energy management strategies for ammonia-hydrogen internal combustion engine hybrid electrical vehicles. *Energy* **2025**, *334*, 137548. [CrossRef]
6. Miao, X.; Zhu, D.; Deng, J.; Dibble, R.; Dong, G.; Li, L. Advances in ion current detection technology for engine applications. *Prog. Energy Combust. Sci.* **2026**, *112*, 101253. [CrossRef]
7. Fang, C.; Ouyang, M.; Yang, F. Real-time start of combustion detection based on cylinder pressure signals for compression ignition engines. *Appl. Therm. Eng.* **2017**, *114*, 264–270. [CrossRef]
8. Xu, H.; Ni, X.; Su, X.; Weng, C.; Yao, C. The effect of ignition intensity and in-cylinder pressure on the knock intensity and detonation formation in internal combustion engines. *Appl. Therm. Eng.* **2022**, *200*, 117690. [CrossRef]
9. Azeem, N.; Beatrice, C.; Vassallo, A.; Pesce, F.; Gessaroli, D.; Biet, C.; Guido, C. Experimental study of cycle-by-cycle variations in a spark ignition internal combustion engine fueled with hydrogen. *Int. J. Hydrogen Energy* **2024**, *60*, 1224–1238. [CrossRef]
10. Zhen, X.; Wang, Y.; Xu, S.; Zhu, Y.; Tao, C.; Xu, T.; Song, M. The engine knock analysis—An overview. *Appl. Energy* **2012**, *92*, 628–636. [CrossRef]
11. Zheng, Z.; Lappas, P.; Shamekhi, A.-M.; Wang, X.; Mikulski, M. Advancements in detecting combustion events through vibration analysis in internal combustion engines: A literature review. *Mech. Syst. Signal Process.* **2025**, *241*, 113539. [CrossRef]
12. Gupta, P.; Kurien, C.; Mittal, M. Computational investigation and analysis of cycle-to-cycle combustion variations in a spark-ignition engine utilizing methane-ammonia blends. *Fuel* **2025**, *386*, 134313. [CrossRef]
13. Rakopoulos, C.D.; Rakopoulos, D.C.; Kosmadakis, G.M.; Zannis, T.C.; Kyritsis, D.C. Studying the cyclic variability (CCV) of performance and NO and CO emissions in a methane-run high-speed SI engine via quasi-dimensional turbulent combustion modeling and two CCV influencing mechanisms. *Energy* **2023**, *272*, 127042. [CrossRef]
14. Wadekar, S.; Janas, P.; Oevermann, M. Large-eddy simulation study of combustion cyclic variation in a lean-burn spark ignition engine. *Appl. Energy* **2019**, *255*, 113812. [CrossRef]
15. Falkenstein, T.; Kang, S.; Cai, L.; Bode, M.; Pitsch, H. DNS study of the global heat release rate during early flame kernel development under engine conditions. *Combust. Flame* **2020**, *213*, 455–466. [CrossRef]

16. Posch, S.; Gößnitzer, C.; Lang, M.; Novella, R.; Steiner, H.; Wimmer, A. Turbulent combustion modeling for internal combustion engine CFD: A review. *Prog. Energy Combust. Sci.* **2025**, *106*, 101200. [CrossRef]
17. Ding, Z.; Truffin, K.; Jay, S. Cause-and-effect chain analysis of combustion cyclic variability in a spark-ignition engine using large-eddy simulation, Part I: From tumble compression to flame initiation. *Combust. Flame* **2024**, *267*, 113566. [CrossRef]
18. Ding, Z.; Truffin, K.; Jay, S. Cause-and-effect chain analysis of combustion cyclic variability in a spark-ignition engine using large-eddy simulation, Part II: Origins of flow variations from intake. *Combust. Flame* **2024**, *267*, 113565. [CrossRef]
19. D'Adamo, A.; Iacovano, C.; Fontanesi, S. Large-Eddy simulation of lean and ultra-lean combustion using advanced ignition modelling in a transparent combustion chamber engine. *Appl. Energy* **2020**, *280*, 115949. [CrossRef]
20. Ji, F.; Meng, S.; Han, Z.; Dong, G.; Reitz, R.D. Progress in knock combustion modeling of spark ignition engines. *Appl. Energy* **2025**, *378*, 124852. [CrossRef]
21. Meng, H.; Zhan, Q.; Ji, C.; Yang, J.; Wang, S. Identification, prediction and classification of hydrogen-fueled Wankel rotary engine knock by data-driven based on combustion parameters. *Energy* **2024**, *308*, 133029. [CrossRef]
22. Duan, X.; Feng, L.; Xia, Y. The mechanism and effect factors of the combustion cycle-to-cycle variations in the spark ignition engine. *Energy Sci. Eng.* **2024**, *12*, 4773–4787. [CrossRef]
23. Deng, B.; Hou, K.; Duan, X.; Xu, Z. The correlation between intake fluctuation and combustion CCV (cycle-to-cycle variations) on a high speed gasoline engine: A wide range operating condition study. *Fuel* **2021**, *304*, 121336. [CrossRef]
24. Maroteaux, F.; Mancaruso, E.; Vaglieco, B.M. Optical and Numerical Investigations on Combustion and OH Radical Behavior Inside an Optical Engine Operating in LTC Combustion Mode. *Energies* **2023**, *16*, 3459. [CrossRef]
25. Xiao, H.; Ying, W.; Chen, A.; Chen, G.; Liu, Y.; Lyu, Z.; Qiao, Z.; Li, J.; Zhou, Z.; Deng, X. Study on the Impact of Ammonia–Diesel Dual-Fuel Combustion on Performance of a Medium-Speed Diesel Engine. *J. Mar. Sci. Eng.* **2024**, *12*, 806. [CrossRef]
26. Zervas, E. Correlations between cycle-to-cycle variations and combustion parameters of a spark ignition engine. *Appl. Therm. Eng.* **2004**, *24*, 2073–2081. [CrossRef]
27. Ozdor, N.; Dulger, M.; Sher, E. Cyclic Variability in Spark Ignition Engines A Literature Survey. *SAE Trans.* **1994**, *24*, 1514–1552.
28. Cao, Y.; Kaiser, E.; Borée, J.; Noack, B.R.; Thomas, L.; Guilain, S. Cluster-based analysis of cycle-to-cycle variations: Application to internal combustion engines. *Exp. Fluids* **2014**, *55*, 1837. [CrossRef]
29. Reyes, M.; Tinaut, F.V.; Giménez, B.; Pérez, A. Characterization of cycle-to-cycle variations in a natural gas spark ignition engine. *Fuel* **2015**, *140*, 752–761. [CrossRef]
30. Wu, Q.; Liang, X.; Zhu, Z.; Cui, L.; Liu, T. Numerical Simulation Research on Combustion and Emission Characteristics of Diesel/Ammonia Dual-Fuel Low-Speed Marine Engine. *Energies* **2024**, *17*, 2960. [CrossRef]
31. Irimescu, A.; Vaglieco, B.M.; Merola, S.S.; Zollo, V.; De Marinis, R. Conversion of a Small-Size Passenger Car to Hydrogen Fueling: Simulation of CCV and Evaluation of Cylinder Imbalance. *Machines* **2023**, *11*, 135. [CrossRef]
32. Ciupek, B.; Brodzik, Ł.; Frąckowiak, A. Research on Carbon Footprint Reduction During Hydrogen Co-Combustion in a Turbojet Engine. *Energies* **2024**, *17*, 5397. [CrossRef]
33. Sfriso, S.; Berni, F.; Fontanesi, S.; D'Adamo, A.; Breda, S.; Teodosio, L.; Frigo, S.; Antonelli, M. Combination of G-Equation and Detailed Chemistry: An application to 3D-CFD hydrogen combustion simulations to predict NOx emissions in reciprocating internal combustion engines. *Int. J. Hydrogen Energy* **2024**, *89*, 161–176. [CrossRef]
34. Menon, S.; Yeung, P.-K.; Kim, W.-W. Effect of subgrid models on the computed interscale energy transfer in isotropic turbulence. *Comput. Fluids* **1996**, *25*, 165–180. [CrossRef]
35. Xin, G.; Xu, Y.; Zhu, H.; Feng, S.; Chen, X. Enhancing the ammonia energy proportion of ammonia hydrogen internal combustion engines through oxygen enriched combustion strategy. *Int. J. Hydrogen Energy* **2025**, *172*, 150603. [CrossRef]
36. Tanaka, S.; Ayala, F.; Keck, J.C. A reduced chemical kinetic model for HCCI combustion of primary reference fuels in a rapid compression machine. *Combust. Flame* **2003**, *133*, 467–481. [CrossRef]
37. Tsurushima, T. A new skeletal PRF kinetic model for HCCI combustion. *Proc. Combust. Inst.* **2009**, *32*, 2835–2841. [CrossRef]
38. Wang, D.; Yu, X.; Li, J.; Yang, W. Effects of Combustion Chamber Shapes on Combustion and Emission Characteristics for the N-Octanol Fueled Compression Ignition Engine. *J. Energy Eng.* **2022**, *148*, 04022011. [CrossRef]
39. Jia, D.; Qiao, J.; Wang, S.; Liu, J.; Guan, J.; Wang, R.; Duan, X. The effect of variable enhanced Miller cycle combined with EGR strategy on the cycle-by-cycle variations and performance of high compression ratio engines based on asynchronous valve opening strategy. *Energy* **2025**, *320*, 135307. [CrossRef]
40. Dai, X.; Zheng, Z. Effects of Piston Shape on the Performance of a Gasoline Direct Injection Engine. *ACS Omega* **2021**, *6*, 34635–34649. [CrossRef]
41. Qin, W.; Shi, J.; Cheng, Q. Numerical simulation study on cycle-to-cycle variations of diesel-natural gas-hydrogen RCCI engine. *Int. J. Hydrogen Energy* **2025**, *118*, 449–456. [CrossRef]
42. Anaclerio, F.; Fornarelli, F.; Masurier, J.-B.; Mounaïm-Rousselle, C. Impact of oxygen enrichment on ammonia combustion in spark-ignition engines under partial load conditions. *Fuel* **2026**, *404*, 135910. [CrossRef]

43. Han, L.; Gong, Y.; Qian, D.; Liu, M.; Ma, H.; Xie, F. Optical investigation of the influence of passive pre-chamber turbulent jet ignition on the combustion characteristics of carbon-free ammonia-hydrogen engines. *Appl. Therm. Eng.* **2025**, *278*, 127200. [CrossRef]
44. Ramirez, F.A.M.; Douasbin, Q.; Dounia, O.; Vermorel, O.; Jaravel, T. Flame-turbulence interactions in lean hydrogen flames: Implications for turbulent flame speed and fractal modelling. *Combust. Flame* **2025**, *273*, 113926. [CrossRef]
45. Shi, X.; Xiong, Q.; Yi, X.; Zhou, X.; Yang, W.; Liu, L.; Zhao, J. Simulation on enhanced combustion characteristics of lean ammonia by pre-chamber turbulent jet-flame ignition strategy in a medium-speed engine. *Appl. Therm. Eng.* **2025**, *280*, 128385. [CrossRef]
46. Wang, T.; Wang, Y.; Zhang, L.; Zheng, Y.; Liu, R.; Wang, C.; Gong, W. Influence of In-Cylinder Turbulence Kinetic Energy on the Mixing Uniformity within Gaseous-Fuel Engines under Various Intake Pressure Conditions. *Energies* **2024**, *17*, 3321. [CrossRef]
47. Fan, B.; Fan, M.; Pan, J.; Yang, W.; Zeng, Y.; Yang, H.; Wu, X. Research and evaluation of turbulent jet ignition mode for improving combustion performance of ethanol rotary engine. *Appl. Therm. Eng.* **2025**, *261*, 125067. [CrossRef]
48. Pei, T.; Chen, F.; Qiu, S.; Wu, D.; Gao, W.; Xu, Z.; Zhang, C. Research on the Intake Port of a Uniflow Scavenging GDI Opposed-Piston Two-Stroke Engine. *Energies* **2022**, *15*, 2148. [CrossRef]
49. Wang, Z.; Zhang, T.; Yang, H.; Wang, S.; Ji, C. Effects of N2 dilution on NH3/H2/air combustion using turbulent jet ignition. *Int. J. Hydrogen Energy* **2024**, *82*, 685–692. [CrossRef]
50. Qiao, J.; Liu, J.; Liang, J.; Jia, D.; Wang, R.; Shen, D.; Duan, X. Experimental investigation the effects of Miller cycle coupled with asynchronous intake valves on cycle-to-cycle variations and performance of the SI engine. *Energy* **2023**, *263*, 125868. [CrossRef]


**Disclaimer/Publisher's Note:** The statements, opinions and data contained in all publications are solely those of the individual author(s) and contributor(s) and not of MDPI and/or the editor(s). MDPI and/or the editor(s) disclaim responsibility for any injury to people or property resulting from any ideas, methods, instructions or products referred to in the content.